Journal of the Mechanical Behavior of Biomedical Materials 168 (2025) 107019

Contents lists available at ScienceDirect

Journal of the Mechanical Behavior of Biomedical Materials

journal homepage: www.elsevier.com/locate/jmbbm

Adhesion of bone cement to porous and nonporous 3D printed surfaces

Caroline Alting [a,*], William R. Walsh [b], Robert Tait [c], Ken Gall [a]

[a] Duke University, USA
[b] University of New South Wales, Australia
[c] Orthopaedic Institute of Henderson, USA

A B S T R A C T

Bone cement is an adhesive commonly used to bond orthopedic implants to bone during a surgical procedure. Total joint replacements such as total knee, hip, shoulder, or ankle arthroplasties have metal or polymer components that are commonly cemented. However, implant failures can occur via debonding at the implant-cement interface, suggesting sub-optimal adhesion of the cement to the implant. In parallel, the orthopedic implant industry is seeing a significant rise in additive manufacturing (AM), which enables the seamless integration of surface porosity enhanced osseointegration in cementless procedures. However, there is a lack of foundational data or understanding of how bone cement adheres to 3D printed surfaces as a function of varying topography. This study evaluates adhesion of cement to clinically relevant printed implant surfaces, porous topographies, and materials. Adhesion strength of cemented samples was tested in shear. Surface porous layers were compared to traditional implant surface finishes (blasted, machined, polished). The impact of 3D printed surface porosity size and depth was also investigated. Testing revealed that the adhesive strength of porous surfaces (26.3 ± 3.1 MPa) was more than double the adhesive strength of all non-porous surfaces (the highest being the as-printed surface with a strength of 11.3 ± 2.5 MPa). The study also demonstrated porosity and layer-depth dependent performance trade-offs, with the best performing group having a 2x2x2 mm^3 unit cell size and 0.50 mm layer depth and a shear strength of 26.31 ± 3.10 MPa. These results provide a foundation for improving designs of emerging 3D printed orthopedic implants that can be both cemented and cementless.

1. Introduction

The application of bone cement, also known as polymethyl methacrylate (PMMA), in orthopedic surgery is a common method to achieve immediate fixation of implants during a surgical procedure (Saha and Pal, 1984). Bone cement interdigitates with the irregularities in the bone and implant surfaces and subsequently cures and hardens to form a mechanical interlock (Vaishya et al., 2013). The alternative to cementing is cementless arthroplasty, wherein an implant's interface directly contacts bone. Known as osseointegration, the interfacing bone eventually grows on- and into the implant to provide long-term secondary fixation (Brånemark, 1983). Despite mixed consensus on the favored surgical method, cementation is often critical for patients with poor bone stock (osteoporotic, pathologic, inflammatory arthritis, and abnormal bone) and remains a significant choice for many procedures (Blankstein et al., 2020; Nam et al., 2019).

Commonly cemented arthroplasties include total ankle (TAA), knee (TKA), total hip (THA), and total shoulder arthroplasty (TSA) (Hannon et al., 2023; Satalich et al., 2022; Refsum et al., 2019; Raiss et al., 2012). Despite generally successful long-term outcomes for all of these procedures, aseptic loosening is a contributing factor for a large percentage of revisions, with some studies citing up to 47 % for TKA (Nam et al., 2019; Gioe et al., 2004; Sharkey et al., 2014), 24 % for THA (Jones and Buckle, 2020), and 30 % for TSA (glenoid specific) (Piper and Neviaser, 2022). Aseptic loosening can be caused by inadequate initial fixation, gradual loss of fixation over time, or particulate induced inflammatory bone degradation, known as osteolysis (Anil et al., 2022). More specifically, studies report debonding at the cement-implant interface as relatively common for the tibial baseplate (TKA) (Hazelwood et al., 2015; Martin et al., 2021; Van Otten and Van Loon, 2022; van Tol et al., 2013; Pittman et al., 2006; Gebert de et al., 2012; Kutzner et al., 2018), femoral stem (THA) (Davies et al., 1996), and glenoid baseplate (TSA) (Sarah et al., 2010). Possible contributions to failure include cement application technique, cement mantle thickness, use of high viscosity cement (HVC) (Kopinski et al., 2016), poor implant design, insufficient implant surface roughness (Van Otten and Van Loon, 2022), patient BMI (Abdel et al., 2015), or interface contamination (Wang et al., 2013). These studies suggest design improvements to include macroscopic pockets, grooves (Van Otten and Van Loon, 2022), or higher surface roughness to increase cement interdigitation (Pittman et al., 2006; Zelle et al., 2011; Zhang et al., 2009).

Cement can interface any of the biomaterials that implants are manufactured from, including titanium alloys, stainless steel, cobalt chrome molybdenum, ceramics, and polyethylene (PE) (Tapscott and

* Corresponding author. Duke University, USA.
E-mail address: caroline.alting@duke.edu (C. Alting).

https://doi.org/10.1016/j.jmbbm.2025.107019
Received 2 October 2024; Received in revised form 19 December 2024; Accepted 16 April 2025
Available online 17 April 2025

Wottowa, 2024). Though metal implant components are more commonly cemented, PE implants, such as the glenoid component of the TSA, are also cemented during surgical reconstruction. Despite successful short-term outcomes, mid- and long-term follow-ups in TSA identify a decrease from 98 % glenoid survivorship at 5 years to approximately 65 % at 10 years (Denard et al., 2013; Gauci et al., 2018; Wallace et al., 1999), suggesting that material properties may also dictate cement adhesion strength and implant survivorship (Denard et al., 2013; Gauci et al., 2018; Kasten et al., 2023).

In recent years additive manufacturing (AM) of these biomaterials has garnered interest for its ability to fabricate intricate, porous, and patient-specific geometries. The titanium alloy, Ti-6Al-4V, is often favored for use in load bearing, non-articulating implants, given its biocompatibility, material properties, and history of successful clinical use. Laser powder bed fusion (L-PBF) is the AM technology typically selected for creating these implants as it enables printing of complex porous structures that are biologically and mechanically advantaged (Singh et al., 2020). These porous structures emulate the porosity of bone (50–90 %) and facilitate osseointegration (Li et al., 2017). In turn, a stable mechanical interlock is created between bone and implant, resulting in improved long-term implant stability (Li et al., 2017; Vijayavenkataraman et al., 2018; Kelly et al., 2019a; Karageorgiou and Kaplan, 2005). Common porous structures include gyroid, octet truss, and stochastic truss-based morphologies. Of these, triply periodic minimal surfaces (TPMS) sheet based morphologies, such as the gyroid structure, possess optimized high-strength and fatigue resistant properties, while maintaining stiffness values within the range of bone (Kelly et al., 2019b, 2021a). Though many traditional subtractive manufacturing methods often have a higher degree of precision for manufactured components, the highly porous and intricate geometries used for many modern Ti-6Al-4V implants make 3D printing superior to subtractive methods. Conversely, AM and L-PBF allow for control over pore size, strut shape, volume fraction, and other porosity parameters at independent spatial locations throughout a part (Mahmoud and Elbestawi, 2019).

Though literature exists on the mechanical strength of common implant surfaces, such as polished or grit-blasted textures, the mechanical interface between cement and surface porosities, especially 3D printed porosities, is poorly studied (van Tol et al., 2013; Pittman et al., 2006; Zelle et al., 2011; Zhang et al., 2009; Cook et al., 1987; Zhang et al., 2008). Cook et al. studied the shear strength of porous coated sintered Ti-6Al-4V alloy specimen and concluded that larger pores have higher interfacial shear strength (25 MPa at 550 μm) than smaller pores (17 MPa at 165 μm) (Cook et al., 1987). Beckmann et al. compared the tensile and torsional strength of cement-bone and cement-porous metal interfaces of trabecular tantalum metal to trabecular bone and concluded that the cement-porous metal interface (14.9 MPa) is stronger than the cement-bone interface (6.3 MPa) in tensile loading (Beckmann et al., 2014). Given that the trabecular metal samples were cut from porous metal stock material, the study lacks comparison of porosities with modulated pore size, morphology, and depth. Exercising this amount of control over implant porosities is only feasible through AM, a technology that was unavailable in prior studies. Kirillova et al. introduced a novel bioresorbable cement that bonds to wet bone and tests this cement on printed Ti-6Al-4V, printed PLA, PEEK (made from stock rods), and cortical and cancellous bone and concluded that shear adhesion is strongest to porous titanium at over 3.5 MPa. However, the study only tested one variation of porosity and did not consider the impact of morphology, size, depth or porosity. Although the mentioned studies analyze adhesion to surface porous structures, they do not comprehensively compare printed surfaces, porosities, and materials (Kirillova et al., 2018).

Given that prior studies have shown that a surface porous layer improves the long-term mechanical interlock with native bone (Kelly et al., 2019a), it is worth analyzing how an implant with a surface porous layer can also improve the cemented interlock. Limited research exists on how cement interacts with AM materials and geometries, and with AM on the rise in the orthopedic implant space, understanding how printed implants interface with bone and cement is crucial (Cuc et al., 2021; Lionberger et al., 2020). In this study, we explore how common implant surface finishes and additively manufactured porosities impact the mechanical interlock between orthopedic implants and bone cement under shear loading. The gyroid was chosen as the clinically-representative porous morphology based on its mechanical properties and established clinical use (Heimbrook et al., 2022a, 2022b). Metal cylindrical plugs were printed via L-PBF using Ti6Al4V powder and tested surfaces were either printed with a surface porous layer or post-processed to achieve a clinically relevant surface finish (Liu et al., 2020). Once samples were assembled with bone cement, they were loaded in shear, which is considered the most physiologically relevant and, along with tension, the weakest mode of failure for bone cement (Dunne, 2008). Surface roughness of the non-porous samples was also characterized to identify if roughness correlates to adhesion strength. In comparing surface topographies and materials, we aim to contribute a deeper understanding of how AM and porous structures impact the stability and longevity of cemented orthopedic implants.

2. Materials and methods

2.1. Sample design

Cylindrical plugs were designed with a radius of 6 mm and a height of 24mm (Kirillova et al., 2018). For the surface porous plugs, the gyroid was applied on one of the flat sides of the cylinder with axially modulated depths using 3DXpert prior to printing. The gyroid porosity was modulated via unit cell size and wall thickness to fall in a range of 60–90 %, which mimics the porosity of bone (Li et al., 2017). Past studies have shown that implants with a porosity within this range showed optimal osseointegration and shear strength in pushout testing of osseointegrated samples (Kelly et al., 2021a). Non-porous plugs were post-processed after printing on one of the flat sides of the cylinder to create samples with different surface roughness. The polymer specimen was the only group that was not printed. Instead, a cylindrical plug of the same dimensions as the 3DP titanium samples was stamped from Vitamin E doped UHMWPE stock material and turned on a lathe to a machine finish. To assemble the final sample, two plugs were adhered together with the cement interfacing the post-processed or porous faces of the respective plug (Fig. 1A). In addition to the sample groups for adhesive shear strength, a plug of pure bone cement was created to compare adhesive shear strength to bulk shear strength. Samples were assigned an acronym and include: porous (POR), as-printed (ASP), blasted (BLA), machined & blasted (MBL), machined (MAC), polished (POL), and machined PE (MPE).

(1) *Non-porous samples:* Samples, except for the ASP sample, were post-processed using various methods to emulate common implant surfaces. BLA surfaces were blasted with 16 grit alumina-oxide using 65 psi air pressure. MBL surfaces were turned on a lathe and then blasted with the same material and settings as the BLA group. MAC surfaces were turned on a lathe. The POL surfaces were sanded with increasingly fine grit paper (200–600 grit) and polished with a buffing wheel and wax until mirror finish was achieved. The MPE sample group was turned on a lathe to achieve a machined surface finish, after the cylindrical plug was stamped from vitamin E doped UHMWPE stock. The bulk cement sample group was formed in a custom mold. The mold was printed via stereolithography (SLA) on a Formlabs 3D printer using Tough 1500 resin. The inside portion of the mold (surface that contacts the bone cement) was covered with Teflon tape to block adhesion of the mold to the cement once the cement was poured into the mold.

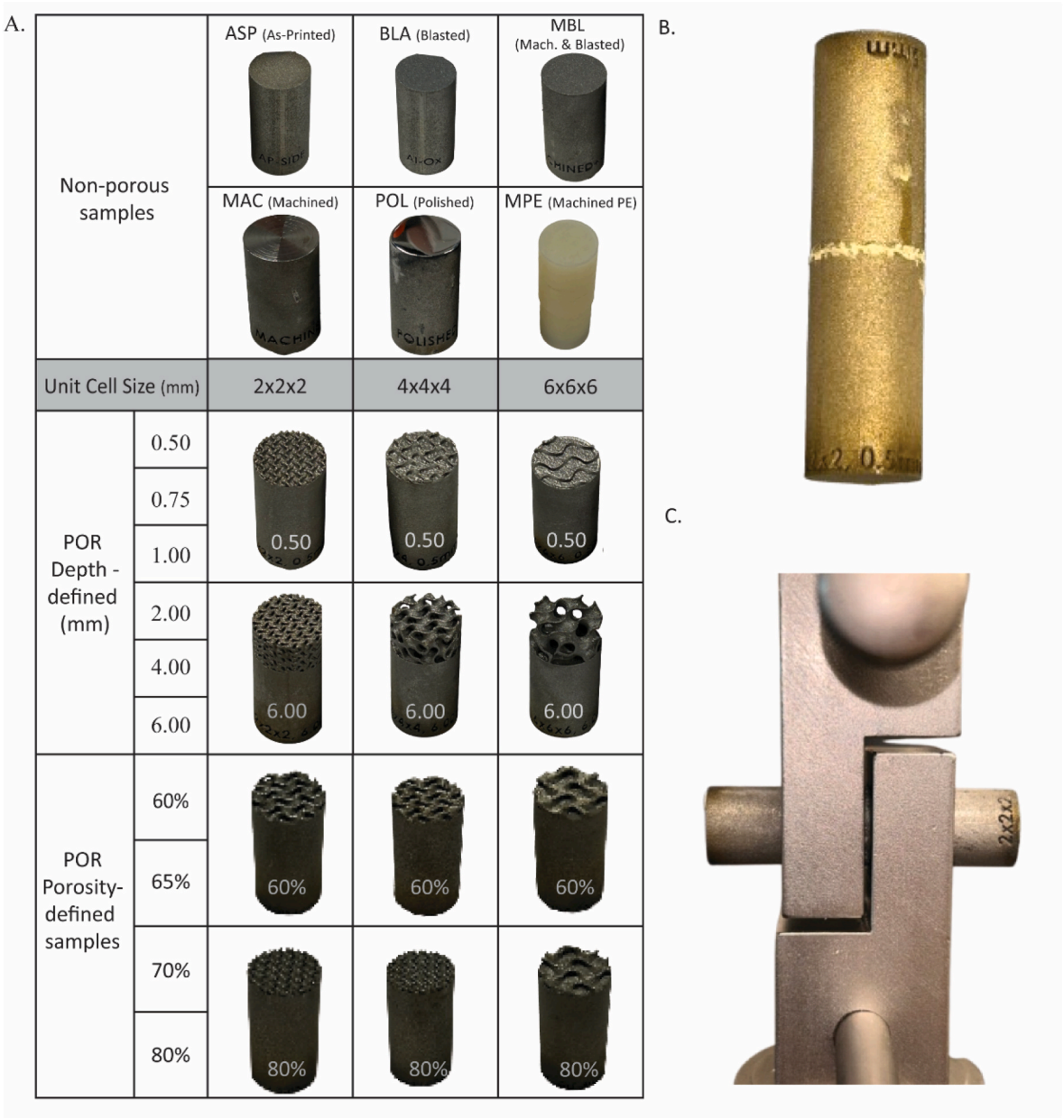

Fig. 1. Representative samples and shear loading test setup. (A) **Non-porous samples** include ASP (as-printed), BLA (blasted), MBL (machined & blasted), MAC (machined), POL (polished), and MPE (machined PE). The specific polymer used was Vitamin E doped UHMWPE. **Depth-defined samples** were given a gyroid surface porosity at 6 different depths (0.50, 0.75, 1.00, 2.00, 4.00, 6.00 mm) and 3 different unit cell sizes (2x2x2, 4x4x4, 6x 6x6 mm^3). Porosity-defined samples were given four different porosities (60 %, 65 %, 70 %, 80 %), which were defined by the wall thickness and three different unit cell sizes (2x2x2, 4x4x4, 6x6 ×6 mm^3). (B) An assembled specimen with two printed plugs adhered together with bone cement (Heraeus Palacos Low-Viscosity) at the substrate surface. In this image, the specimen with a 2x2x2 mm^3 unit cell size and 0.50 mm depth is shown. (C) Shear testing set-up showing the machined grips that hold the cylindrical specimen and isolate the substrate-cement interface.

(2) *Depth-defined samples:* Samples were defined by their unit cell size and depth of gyroid. The unit cell sizes included 2x2x2, 4x4x4, and 6x6x6 mm^3. These 3 variations included the following depths: 0.50, 0.75, 1.00, 2.00, 4.00, and 6.00 mm. A wall thickness of 0.25 mm was used for all samples. Pore size was approximated through nTopology (Ver 4.20.2, New York, USA) and is tabulated in Table 1.

(3) *Porosity-defined samples:* Samples were defined by their unit cell size and porosity of the surface gyroid, which was modulated by changing the wall thickness of each sample group. The included porosities were 60 %, 65 %, 70 %, and 80 %. Pore size was approximated through nTopology (Ver 4.20.2, New York, USA) and is tabulated in Table 1, along with corresponding wall thickness.

2.2. Additive manufacturing

The metal plugs were printed via laser powder bed fusion (L-PBF) on a 3D Systems DMP ProX 320 metal printer using Ti-6Al-4V grade 23 ELI powder and in an inert Argon atmosphere with optimized printing and laser parameters (Kelly et al., 2019b). All samples, except for ASP and BLA samples, were printed with the substrate surface parallel (surface normal perpendicular) to the build-plate. The ASP and BLA samples were printed with the substrate surface perpendicular (surface normal parallel) to the build-plate for a true representative "as-printed" surface.

Table 1
Designed and intrinsic properties of porous cylindrical plugs for the depth and porosity defined studies.

Study	Unit Cell Size (mm^3)	Wall Thickness (mm)	Pore Size – Approximate (μm)	Porous Layer Depth (mm)	Target Porosity (%)	CAD Porosity (%)
Depth Defined	2x2x2	0.25	720	0.50	65	64.7
				0.75		64.7
				1.00		64.8
				2.00		64.8
				4.00		64.6
				6.00		64.7
	4x4x4	0.25	1400	0.50	82	82.2
				0.75		81.3
				1.00		82.0
				2.00		82.0
				4.00		82.1
				6.00		82.1
	6x6x6	0.25	2300	0.50	90	90.2
				0.75		88.3
				1.00		87.3
				2.00		88.6
				4.00		88.0
				6.00		88.2
Porosity Defined	2x2x2	0.29	700	1.00	60	60.1
		0.25	720		65	64.8
		0.21	740		70	70.2
		0.14	780		80	80.1
	4x4x4	0.57	1160	1.00	60	60.0
		0.50	1220		65	64.7
		0.42	1300		70	70.1
		0.28	1440		80	79.9
	6x6x6	0.83	1600	1.00	60	59.9
		0.70	1800		65	65.6
		0.61	2000		70	69.6
		0.41	2200		80	79.6

Surfaces printed "upskin" or in the +Z direction have less unmelted powder particles attached and, thus, have a lower surface roughness and are not representative of most printed surfaces. To optimize mechanical properties, the build-plate was post-processed via Hot Isostatic Pressing (HIP) at 1650 °F at 14,750 psi for 130 min. Samples were cut from the plate via electrical discharge machining (EDM).

2.3. Sample assembly

Heraeus Medical Palacos Low-Viscosity bone cement was manually mixed and applied according to the manufacturing instructions in a room at 22 °C. The only deviation from the manufacturing instructions is that instead of mixing the entire package of powder with the entire vial of liquid at once, the powder and liquid were measured out in a 2:1 ratio of grams to milliliter using a calibrated scale and pipette. This was done to prevent excessive waste as only a few samples were able to be assembled within the working time of the cement. The cement was mixed for 30 s and then applied with a spatula to the top sample face of each plug once the cement became "doughy." Two of the same plugs were then pressed together using light finger pressure for 30 s. Any excess cement that was expelled beyond the sample face was wiped away. Typically, 3 samples (6 plugs) were cemented and assembled at a time. Assembled samples were then left to set for at least 24 h (Fig. 1B).

2.4. Microscopy images

Representative samples were imaged using a ThermoFisher Apreo™ 2 scanning electron microscope before and after shear testing. Images were taken at a working distance of approximately 7 mm with a voltage of 2.00 kV and current of 25 pA. Representative samples were also imaged after shear testing to evaluate fracture surfaces with an Olympus Life Science SZ61 stereo optical microscope with the Olympus SC50 camera.

2.5. Surface characterization

The surface line (arithmetic mean deviation, R_a) and area roughness (arithmetic mean height, S_a) of each sample group were measured with a Filmetrics Profilometer Standard with a 100 mm × 100 mm stage under a 10× Nikon DI objective lens using white light interferometry. Scanning was conducted at a cut-off wavelength of $\lambda_c = 0.25$ μm. Four plugs were randomly chosen and scanned for each sample group. The porous sample group was not measured as it has a macroscopic porous topography.

2.6. Shear testing

Assembled samples (n = 4 per group) were tested in shear on a TestResources 910LX25 testing frame with a 25 kN load cell. The crosshead displacement rate was 2 mm/min and data acquisition speed was 40 Hz for all measurements. Custom shear fixtures, machined from stainless steel and aluminum stock, held the cylindrical samples and isolated the cement-metal interface (Fig. 1C). Shear strength was determined by dividing the peak load at failure by interfacial area of the sample surface. Interface stiffness was calculated by dividing shear strength by displacement at failure (MPa/mm).

2.7. Statistical analysis

The sample size is 4 samples (2 cylinders adhered together with bone cement) per group. Mechanical data of shear strength of bulk cement, representative porous, and non-porous groups is presented as the average and standard deviation. Surface roughness of non-porous groups and shear strength are correlated using the coefficient of determination (R^2). One-way ANOVA and Games Howell post-hoc tests with $p < 0.05$ were used to examine differences in shear strength amongst (1) sample groups with varying surface topographies (bulk cement, porous, and non-porous), (2) sample groups with varied depths of porosities, and (3) sample groups with different porosities. All statistical analysis was

computed with SPSS (IBM Ver 29).

3. Results and discussion

3.1. Microscopy images and surface roughness

Fig. 2 displays representative SEM images of the samples and their corresponding surfaces. Below each sample descriptor is the surface area (S_a) and line roughness (R_a) in μm. The POR and ASP samples show the characteristic roughness of an unprocessed surface typical of the L-PBF process. The round beads apparent in the images are partially melted powder particles that were not fully incorporated in the melt-pool of the laser-path. It was expected that the increased surface roughness of the POR and ASP samples would increase adhesion to bone cement. The BLA (4.3 ± 0.2 μm) and MBL (4.0 ± 0.4 μm) samples show similar surface topographies and roughness values. Though blasting is intended to produce a rough surface, the BLA and MBL surfaces have a lower S_a than ASP surfaces (6.1 ± 1.1 μm). The MAC (0.6 ± 0.3 μm) and POL (0.04 ± 0.01 μm) samples show smooth surfaces and S_a values that are markedly lower than the ASP, MAC, and MBL surfaces. Note that the MPE surface (1.8 ± 0.6 μm) has a rougher surface than the MAC (machined Ti-6Al-4V) samples. S_a values are detailed in Fig. S1 of the supplementary materials.

Fig. 3 displays post-testing microscope (optical and SEM) images and the respective failure mode that each sample group experienced. Failure at a bonded interface can be described as either an adhesive or cohesive failure mode (Kirillova et al., 2018; Bou-Francis and Ghanem, 2017). Adhesive failure indicates that failure occurred on one interface of the adhesive, which is left on only one side of the substrate. Cohesive failure indicates that failure occurred at the bulk layer of the adhesive itself, leaving the adhesive on both sides of the substrate. Strong chemical bonds and mechanical interlock between the substrates and adhesive are generally the cause for a cohesive failure mode.

Non-porous sample groups failed via an adhesive mode, where the cement completely debonded from one substrate and remained on the other. In contrast, the POR samples exhibited a cohesive failure mode, with cement remaining on both substrates. As seen in Fig. 3, the POR samples display the roughest cement rupture surface, indicating cement penetration into the pores and bulk cement failure rather than adhesive shear failure. Partially melted and adhered powder particles that are inherent to the L-PBF process can be seen embedded in the ruptured cement, indicating that these were stripped from the metal substrate.

The ASP group displays the negatives of the rough as-printed surface, along with particles that were stripped from the metal substrate. Generally, more embedded particles were observed in the cement of the ASP sample group than any other group. The dislodgement of the particles from the metal substrate supports the idea of a strong mechanical cement-metal bond. BLA and MBL samples show similar cement rupture surfaces, featuring rough impressions of the blasted metal substrates in the remaining cement. A few powder particles and metal debris were also observed in the cement for these rough blasted groups. MAC, POL, and MPE all show similarly smooth impressions of their respective substrates. Micropores were observed in the cement of the POL group and can be attributed to mixing of cement in a non-vacuum environment. The observed difference in failure modes of porous and non-porous samples provides a foundation to the mechanical results (Fig. 4), given that shear strength for porous samples (>25 MPa) is higher than that of non-porous samples (<15 MPa).

3.2. Shear strength behavior of porous and non-porous samples

Fig. 4A displays representative force-displacement curves of bulk cement, one representative POR (2x2x2 mm^3 unit cell size and 0.50 porous depth), and non-porous specimens. All curves show a linear elastic region, followed by peak load and failure. The bulk cement sample shows the highest force at failure at 3100 N at 2.20 mm

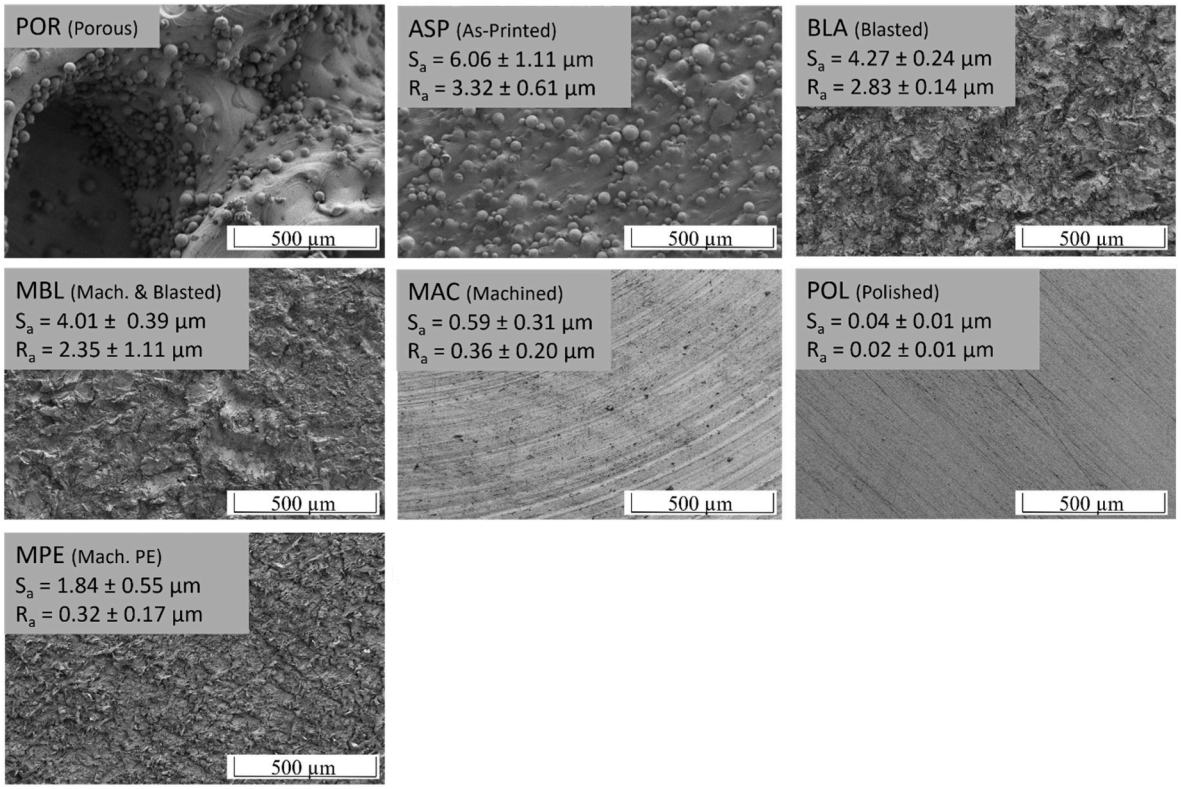

Fig. 2. SEM images of surface topography of 1 representative porous (POR) sample (2x2x2 mm^3 unit cell size, 0.50 depth) and non-porous samples. Below each description (except for the POR sample), is the surface area (S_a) and line (R_a) roughness (μm). POR and ASP images showcase the partially adherent powder particles that are inherent to the powder bed fusion (PBF) printing process.

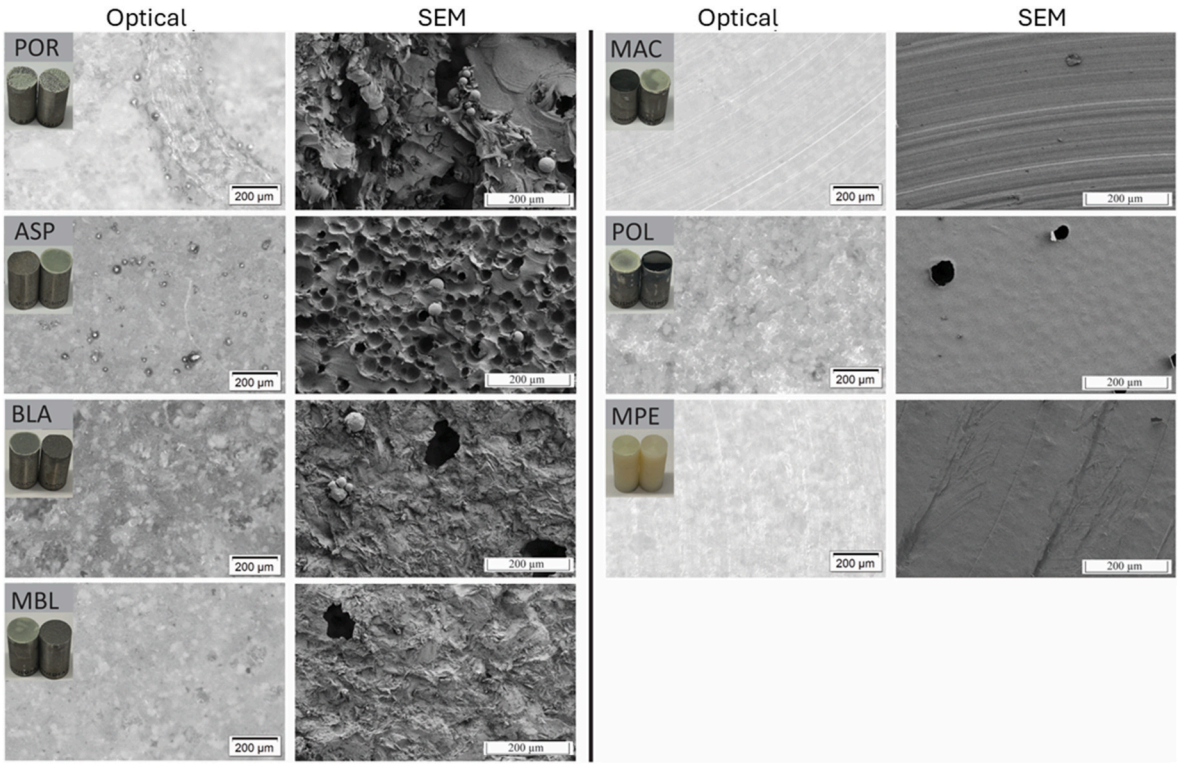

Fig. 3. Optical microscope (left column) and SEM images (right column) of post-testing sample surfaces of 1 representative POR sample (2x2x2 mm unit cell size, 0.5 mm porous layer depth) and non-porous samples. POR samples show cohesive or bulk failure mode, meaning cement is left on both substrates. Non-porous samples show an adhesive failure mode, meaning cement is left on only one of the two substrates.

displacement and serves as a reference to the upper limit of the bulk shear strength as fabricated here. No indentation or deformation of the plugs was observed apart from the line of shear failure at the cement interface. The POR sample features the second highest force at failure with 2532 N at 0.46 mm displacement.

The "rough" non-porous samples (ASP, BLA, and MBL) show forces at failure in similar ranges from 700 to 1100 N. The curves for BLA and MBL samples feature kinking, which suggests partial debonding prior to complete adhesive failure. The ASP sample features the highest force at failure among the non-porous sample groups. The "smooth" non-porous samples, MAC, POL, and MPE, show forces at failure in similar ranges from 100 to 300 N.

Fig. 4B presents average shear strength and standard deviation of non-porous specimens, one representative porous specimen, and the bulk bone cement specimen. The bulk bone cement plug, with a shear strength of 27.3 ± 1.6 MPa serves as a reference to the upper limits of the cement's inherent shear strength. A representative POR specimen (2x2x2 mm^3 unit cell size, 0.50 mm depth) compares the effect of porosity on shear strength relative to non-porous specimen. POR samples show an average adhesive shear strength of 26.3 ± 3.1 MPa, which is slightly lower than the shear strength of the pure bone cement in bulk form. No significant difference was established between the bulk cement and POR groups. Fig. 4D presents the interface stiffness in MPa/mm and standard deviation of the bulk cement, POR, and non-porous groups.

Among the "rough" non-porous groups, the ASP, BLA, and MBL specimens exhibit a shear strength that is approximately 50 % of the POR group. Specifically, the ASP specimen, the roughest among the non-porous sample groups, averages 11.3 ± 2.5 MPa, which is 43 % of POR strength. The BLA and MBL specimens, with similar but slightly smoother surfaces, show average shear strengths of 9.7 ± 2.8 and 10.5 ± 3.8 MPa, respectively. Among the "smooth" non-porous groups, the MPE, MAC, and POL specimens showed lower strengths: 1.1 ± 0.2, 1.8 ± 0.9, and 0.4 ± 0.2 MPa respectively. No significant difference was established amongst the "rough" non-porous sample groups (ASP, BLA, MBL), as well as amongst the "smooth" non-porous sample groups (MPE, MAC, POL). The shear strength of the POR group is significantly ($p < 0.05$) higher than that of any of the non-porous groups (excluding the bulk cement group).

Comparison of adhesive shear strength between bulk cement, POR, and non-porous groups highlights that even a slight porosity depth significantly ($p < 0.05$) improves mechanical strength of adhered plugs in shear loading. Note that the shear strength of the POR specimen closely approaches bulk cement shear strength limits with no statistically significant difference. This result, along with the images of the rough rupture surface of the porous sample in Fig. 3., display the cohesive failure mode that the porous sample groups experienced. Instead of peeling or debonding at the adhesive interface, the cement ruptured in bulk. The pores function as a scaffold to support the bulk cement and the multi-directional surfaces of the pores convert shear loads into complex local stress states that cause the cement failure mode to act more like bulk failure rather than adhesive shear failure. Furthermore, as the cement interdigitates with the pores, the adhered surface area increases, thus requiring more energy to rupture the interface. In contrast, non-porous surfaces experience mostly uninterrupted shear stresses as there is less or no cement penetration. This results in adhesive debonding and cement peeling or detaching from one sample plug. Furthermore, many factors play into the quality and strength of the cement bond including surgeon technique, vacuum vs. hand-mixing, pressurization of application, atmospheric temperature, contamination of the target bone, etc. However, these results suggest that a porous surface can result in a more forgiving implant which would decrease the relevance of these factors during surgery. As they were not considered in this study, it is worth pursuing additional studies to compare the relevance of these factors in porous vs non-porous implants.

Fig. 4C illustrates the positive correlation ($R^2 = 0.8896$) between surface roughness and adhesive shear strength among non-porous groups for a given material. The ASP specimen, with the highest S_a at 6.1 ± 1.1 µm, shows an average shear strength of 11.3 ± 2.5 MPa.

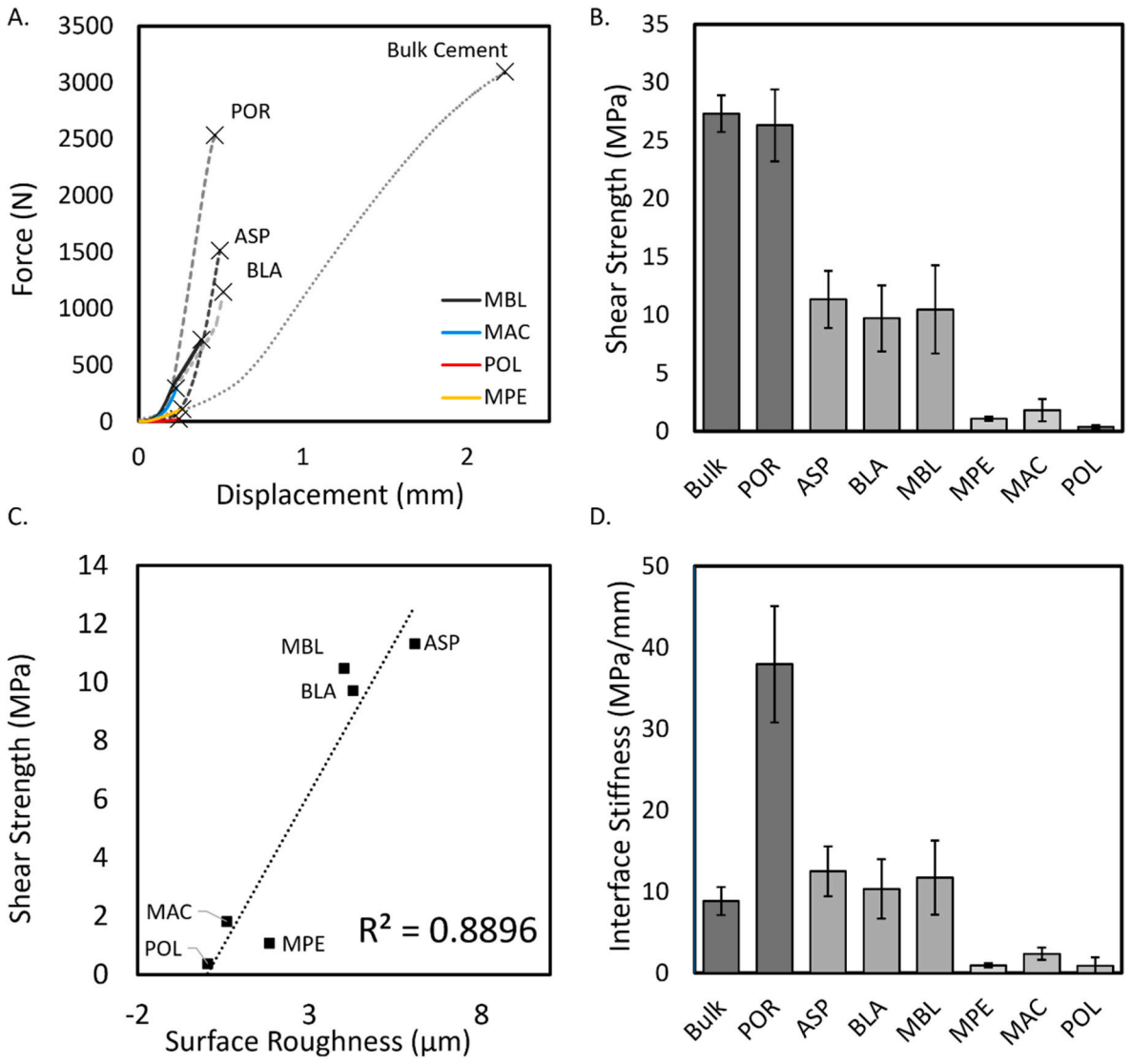

Fig. 4. (A) Representative force-displacement curves of bulk cement, 1 representative porous sample (2x2x2 mm^3 unit cell size, 0.50 mm depth), and non-porous samples. These curves showcase a linear elastic region, followed by peak load and adhesive failure. (B) Plot of average shear strength (MPa) of bulk cement, 1 representative porous sample (2x2x2 mm^3 unit cell size, 0.50 mm depth), and non-porous samples. The data show a significant difference between POR and all non-porous groups (excluding the bulk cement group). (C) Plot of surface roughness vs. average shear strength of non-porous samples. The trendline shows $R^2 = 0.8896$. (D) Plot of average interface stiffness (MPa/mm) of the samples. The POR group shows the highest interfacial stiffness at 38 MPa/mm.

Though machining & blasting is the industry standard, inherent roughness from L-PBF (as-printed surfaces) yields comparable cement-implant interface strength. As orthopedic implant manufacturing adopts AM, removing blasting as an extra post-processing step and opting instead for as-printed surfaces may be a cost- and time-efficient path to better results.

Material chemistry may also play a role in how cement adheres to an implant, which is shown by the higher shear strength of the machined Ti-6Al-4V (MAC) vs. the machined PE (MPE) group. Despite having a lower surface roughness, machined Ti-6Al-4V has a higher average shear strength than machined PE (0.6 ± 0.3 µm and 1.8 ± 0.6 MPa for machined Ti-6Al-4V vs. 1.8 ± 0.5 µm and 1.1 ± 0.2 MPa for machined PE) as seen in Fig. 4C. These results indicate that both mechanical and chemical bonding contribute to cement adhesion strength. Adhesive bonding to PE may be more difficult due to the inert and non-polar material properties of PE (Oosterom et al., 2006). In contrast, titanium is known to form a titanium dioxide (TiO_2) layer at the surface, which could contribute to a higher bonding affinity between the cement and metal (Kirillova et al., 2018; Cuc et al., 2021; Bruni et al., 2005). To draw firmer conclusions about bonding to metal vs. polymer, additional mechanical and chemical testing would be necessary.

3.3. Effects of porosity depth

Fig. 5A presents the adhesive shear strength of depth-defined porous samples and evaluates the optimal depth of a surface porous layer across 6 different depths (0.50, 0.75, 1.00, 2.00, 4.00, 6.00) and 3 different unit cell sizes (2x2x2, 4x4x4, and 6x6x6 mm^3), which correspond to 3 different approximated pore sizes (720, 1400, 2300 µm). Fig. 5B presents the same data in tabular format. A significant difference ($p < 0.05$) was found among the small (2x2x2 mm^3) and large (6x6x6 mm^3) unit cell sizes, but not among the intermediate unit cell size (4x4x4 mm^3). One sample (4 × 4x4 mm^3 - 0.50 mm depth) broke before testing, reducing the sample size for the 4x4x4 mm^3 - 0.50 depth sample group from n = 4 to n = 3.

For thin layers, the smallest pore size (720 µm corresponding to the 2x2x2 mm^3 unit cell size) achieved the highest shear strength of 26.3 ± 3.1 MPa at 0.50 mm. However, strength decreased as depth increased

A.

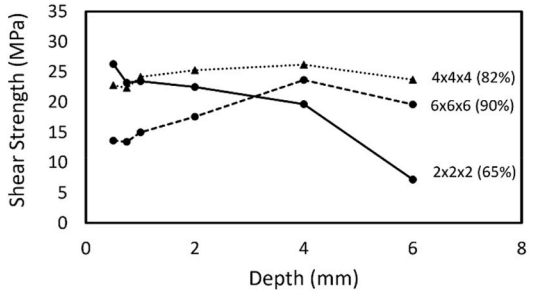

B.

Depth (mm)	Shear Strength (Mpa)		
	2x2x2 mm^3	4x4x4 mm^3	6x6x6 mm^3
0.50	26.31 ± 3.10	22.78 ± 1.86	13.61 ± 1.66
0.75	23.22 ± 3.84	22.33 ± 2.88	13.41 ± 1.76
1.00	23.44 ± 4.37	24.16 ± 1.72	14.99 ± 3.42
2.00	22.52 ± 4.18	25.26 ± 1.68	17.58 ± 4.83
4.00	19.63 ± 5.42	26.17 ± 1.72	23.66 ± 2.09
6.00	7.17 ± 3.98	23.69 ± 2.39	19.62 ± 7.68

C.

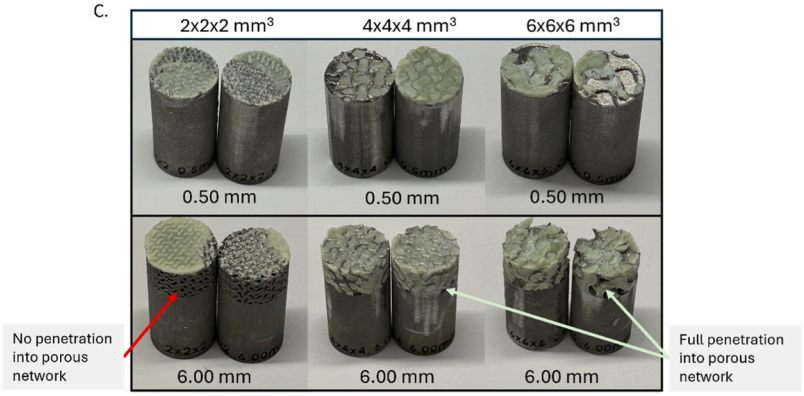

Fig. 5. (A). Plot of shear strength of depth-defined porous samples with three different unit cell sizes (2x2x2, 4x4x4, 6x6x6 mm^3 unit cell size). Inherent to fixing unit cell size and wall thickness of the gyroid, the depth-defined porosity results in 65 %, 82 %, and 90 % for the 2x2x2, 4x4x4, and 6x6x6 mm^3 unit cell sizes, respectively. (B) Table of shear strength of depth-defined porous samples. (C) Post-testing images of depth-defined porous groups, showcasing the minimum and maximum depths used, 0.50 mm and 6.00 mm. It is important to note the cut-off in cement penetration for deeper depths for the smaller (2x2x2 mm^3) unit cell size.

and saw a statistically significant ($p < 0.05$) decrease at 6 mm. As seen in Fig. 5B, at 0.50, 0.75, 1.00, 2.00, 4.00, and 6.00 mm depths, the smallest pore size had strengths of 26, 23, 23, 22, 20, and 7 MPa, respectively. The intermediate pore size (1400 μm corresponding to the 4x4x4 mm^3 unit cell size) showed a stable trend across all depths and peaked at 26.2 ± 1.7 MPa at the 4 mm depth. At 0.50, 0.75, 1.00, 2.00, 4.00, and 6.00 mm depths, the intermediate pore size had shear strengths of 23, 22, 24, 25, 26, and 24 MPa, respectively. No significant difference was found amongst the depths of the 4x4x4 mm^3 unit cell size. The largest pore size (2300 μm corresponding to the 6x6x6 mm^3 unit cell size) showed the lowest strengths across the depths. The peak strength of 23.7 ± 2.1 MPa at 6.00 mm was significantly higher ($p < 0.05$) than at depths of 0.50 and 0.75 mm. At 0.50, 0.75, 1.00, 2.00, 4.00, and 6.00 mm depths, the largest pore size had shear strengths of 14, 13, 15, 16, 24, and 20 MPa, respectively.

These results highlight a trade-off between pore size and cement contact surface area, specifically related to the depth of the porous layer. Increasing porous layer depth for the smallest pore size significantly ($p < 0.05$) decreases shear strength at the cement-implant interface. Post-testing images in Fig. 5B Support this finding by showing a maximum amount of cement penetration into the porous layer. In the images, cement only penetrates the porous layer by about 1 mm, despite the increasing depth of the porous layer. This can be attributed to the smaller pores of the 2x2x2 mm^3 unit cell size preventing cement penetration beyond ~1 mm. Theoretically the strength should increase with porous network depth as the interfacial contact area between cement and pores increases. However, a possible reason as to why strength does not increase could be related to the distancing of the solid-porous interface from the cement-porous interface. The solid-porous interface – where the porous network meets the solid portion of the cylinder – acts like a backing that pressurizes the cement into the entire porous volume. In contrast, the deeper the surface porous layer, the less of a "backing" there is to pressurize the cement into the total porous volume. These results could change if different techniques are used, for example: pressurized cement application, controlled volume of cement, different test method, etc. Still, the 2x2x2 mm^3 unit cell size performs best at 0.50 mm depth out of all the tested groups, suggesting that only a relatively thin layer of surface porosity is sufficient to significantly increase cement adhesion to an implant.

In contrast, the larger pore sizes (4x4x4 and 6x6x6 mm^3 unit cell sizes) allow for cement penetration into the total porosity volume for all depths. Both display a positive trend between increasing depth and shear strength, up to the 4 mm depth. As the cement penetrates the pores, the porous network acts as a scaffold that strengthens the pore-cement unit. The intermediate pore size (4x4x4 mm^3 unit cell size) exhibits a stable trend in strength across increasing depths, which is supported by the lack of significant difference between these shear strengths. This suggests that performance of the intermediate pore size is less sensitive to the depth of the porous layer. The intermediate pore size "scaffolding" is optimized by balancing the interfacial contact area between the intermediate porous network and penetrating bone cement. In contrast, the large pore size (6x6x6 mm^3 unit cell size) has significant differences between strengths as related to the porous layer depth. This is most likely caused by the pores being too large and not providing enough "scaffolding" or interfacial contact area between the porous network and the penetrating cement. Although this large scaffold size is good for storage of therapeutic biologics and biological ingrowth (Kelly et al., 2021b), it is not as effective for cement adhesion compared to finer porous structures when the implant can only contain a thin sub 2 mm porosity layer.

These findings indicate that even a thin surface porous layer can have a significant impact on the adhesive shear strength. This is especially relevant for implants with more constrained surface areas or joints where bone resection is limited. One such example is the Total Ankle Arthroplasty (TAA) in which implant surface area and thickness are relatively constrained considering the small size of the ankle joint. Furthermore, these results determine that smaller unit cell sizes require shallower depths of the surface porous layer as pressurization of the

cement application and distribution into the entire porous network is lost. A limitation of this study is that volume and pressurization of the applied cement was not controlled for.

3.4. Effects of porosity with a fixed 1 mm layer depth

Fig. 6 Shows the adhesive shear strength of porosity-defined samples and evaluates the optimal porosity at a given unit cell size when the layer depth is fixed at a depth of 1 mm. The porosities were chosen as 60 %, 65 %, 70 %, and 80 % to emulate the porosity of trabecular bone (Li et al., 2017). These porosities were varied across the same unit cell sizes as in the previous depth-defined study: 2x2x2, 4x4x4, and 6x6x6 mm^3. The smallest unit cell size, 2x2x2 mm^3, performed the best across all porosities and peaked at 80 % at 31.2 ± 1.9 MPa. The intermediate unit cell size, 4x4x4 mm^3, followed a similar trend and had strengths slightly below that of the 2x2x2 mm^3 groups across all porosities. The 4x4x4 mm^3 groups peaked at 80 % at 27.9 ± 4.7 MPa. The 6 × 6x6 mm^3 unit cell size again followed a similar trend. However, the shear strength at all porosities was weaker than both 2x2x2 mm^3 and 4x4x4 mm^3 sample groups and peaked at 80 % at 22.2 ± 3.0 MPa. The only group that saw a significant difference ($p < 0.05$) in shear strength was the 6x6x6 mm^3 unit cell size between the 80 % porosity and 60 % and 65 % porosities, respectively.

The 2x2x2 mm^3 group experienced a minimal difference in shear strength of 0.6 MPa between 60 % and 80 % porosity. The 4x4x4 mm^3 group experienced a difference of 1.9 MPa. The 6x6x6 mm^3 group experienced the most significant ($p < 0.05$) increase in shear strength between 60 % and 80 % porosity, at a difference of 4.3 MPa. These differences show that porosity has a more significant effect on larger unit cell sizes (6x6x6 mm^3).

Considering that the smallest unit cell size (2x2x2 mm^3) had the highest shear strengths across all porosities, followed by the intermediate (4x4x4 mm^3) and then the largest unit cell size (6x6x6 mm^3) could indicate that unit cell size may have more dominating effects on shear strength than porosity. The weaker shear strength of the larger unit cell size can be attributed to the porous network (6 mm periodicity) being too large relative to the layer thickness (1 mm). This results in less penetration of cement into the porous network and a decreased interfacial surface area as compared to the smaller unit cell sizes.

Though this range represents porosity used in implants, the range does not provide an encompassing scope of how porosity affects interfacial strength. It would be valuable to increase the porosity range in future studies to identify if there remains a positive correlation between porosity and strength or if there is a cut-off or trade-off between porosity and strength. However, it is interesting to note that the "bulk" mechanical properties of porous structures vary widely over this porosity range, where you can see a strength decrease of ~60 MPa from 60 % porosity to 80 % porosity (Kelly et al., 2019b). This trend in material strength is not evident in the adhesion strength of cement to a 3D printed porous surface over the same variation in porosity. This highlights the complexity of the local mechanics of adhesion to the porous surface, which is an interplay between mechanical and chemical factors, as well as a blend of properties of both the cement and porous metal structures.

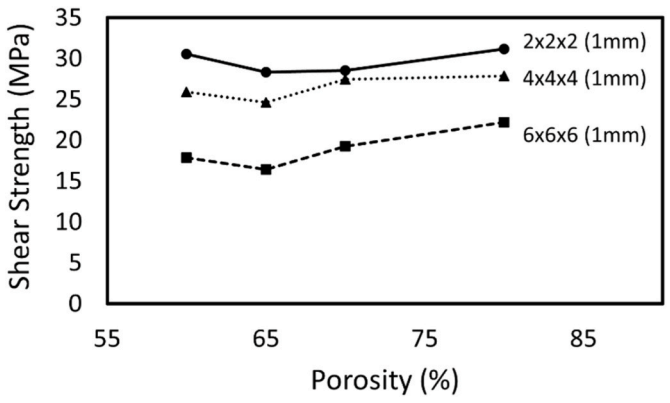

Fig. 6. Plot of shear strength of porosity-defined samples with three different unit cell sizes (2x2x2, 4x4x4, 6x6x6 mm^3 unit cell size). The tested, clinically relevant porosities include 60 %, 65 %, 70 %, and 80 %. All porosity-defined samples have a surface porous layer that is 1.00 mm deep.

3.5. Limitations

Though this study explores the adhesive shear strength of different surfaces and porosities, limitations to the study design inhibit true representation of what an implant experiences in-vivo. One limitation is that the performed shear testing is not reflective of the complex and multi-axis loading that an implant experiences. Dynamic fatigue testing more accurately portrays the repetitive loading in everyday activities over time. Furthermore, only one type of cement was used and only tested with metal interfaces and not bone interfaces. Testing was also performed at room temperature in ambient air. In future studies, additional features such as a broader range of porosity, pore morphologies, and loading modes of the full bone-cement-implant system will be explored.

4. Conclusions

This study explores the effects of surface roughness, material, porosity, and porosity depth on the shear strength of the cement-substrate interface of 3D printed Ti-6Al-4V substrates. Though common cement-interfacing implant surfaces include non-porous machined, blasted, or polished surfaces, the present results reveal a significantly higher cement adhesion strength to porous surfaces than to non-porous surfaces. The main results can be summarized as follows.

1. Cement adheres to porous samples with approximately twice the strength than to non-porous rough samples.
2. Among the non-porous samples, cement adheres to ASP, BLA, and MBL samples approximately 5 times better than to POL, MAC, and MPE surfaces. As orthopedic implant manufacturing adopts AM, removing blasting as an extra post-processing step and opting instead for just as-printed surfaces may be a cost- and time-efficient path to better results.
3. Choice of implant material impacts cement adhesion. Machined Ti-6Al-4V (MAC) has a higher adhesion strength than machined PE (MPE) despite the latter being rougher.
4. Pore size and porous layer depth are related in terms of shear adhesion strength. A smaller pore size (~720 μm) performs better at smaller depths (0.50 mm) and a larger pore size (~2300 μm) performs better at larger depths (4.00–6.00 mm). An intermediate pore size (1400 μm) performs consistently well across multiple depths (0.50–6.00 mm), making the 4x4x4 mm^3 unit cell size favorable for more applications.
5. At a fixed porous layer depth of 1 mm, the 2x2x2 mm^3 unit cell size had the highest shear adhesion strength at four different porosities (60 % 65 %, 70 %, 80 %).

These results highlight the impact that porous structures can have on adhesive strength at the cement-implant interface. The findings of this study will hopefully influence the design and development of implants that can be both cemented or cementless.

CRediT authorship contribution statement

Caroline Alting: Writing – review & editing, Writing – original draft, Visualization, Validation, Methodology, Investigation, Formal analysis, Data curation, Conceptualization. **William R. Walsh:** Writing – review & editing, Visualization, Validation, Supervision, Methodology. **Robert**

Tait: Writing – review & editing, Validation, Supervision, Investigation, Conceptualization. **Ken Gall:** Writing – review & editing, Supervision, Resources, Project administration, Funding acquisition, Conceptualization.

Declaration of competing interest

The authors declare the following financial interests/personal relationships which may be considered as potential competing interests: Ken Gall reports a relationship with restor3d that includes: board membership, employment, and equity or stocks. If there are other authors, they declare that they have no known competing financial interests or personal relationships that could have appeared to influence the work reported in this paper.

Appendix A. Supplementary data

Supplementary data to this article can be found online at https://doi.org/10.1016/j.jmbbm.2025.107019.

Data availability

Data will be made available on request.

References

Abdel, M.P., Bonadurer, G.F., Jennings, M.T., Hanssen, A.D., 2015. Increased aseptic tibial failures in patients with a BMI ≥35 and well-aligned total knee arthroplasties. J. Arthroplast. 30, 2181–2184.

Anil, U., Singh, V., Schwarzkopf, R., 2022. Diagnosis and detection of subtle aseptic loosening in total hip arthroplasty. J. Arthroplast. 37, 1494–1500.

Beckmann, N.A., et al., 2014. Mechanical properties of a cemented porous implant interface. Acta Orthop. 85, 531–537.

Blankstein, M., Lentine, B., Nelms, N.J., 2020. The use of cement in hip arthroplasty: a contemporary perspective. JAAOS J. Am. Acad. Orthop. Surg. 28, e586.

Bou-Francis, A., Ghanem, A., 2017. Standardized methodology for in vitro assessment of bone-to-bone adhesion strength. Int. J. Adhes. Adhes. 77, 96–101.

Brånemark, P.I., 1983. Osseointegration and its experimental background. J. Prosthet. Dent 50, 399–410.

Bruni, S., et al., 2005. Effects of surface treatment of Ti–6Al–4V titanium alloy on biocompatibility in cultured human umbilical vein endothelial cells. Acta Biomater. 1, 223–234.

Cook, S.D., et al., 1987. Optimum pore size for bone cement fixation. Clin. Orthop. Relat. Res. 223, 296.

Cuc, S., et al., 2021. Adhesion between biocomposites and different metallic structures additive manufactured. Coatings 11, 483.

Davies, J.P., Tse, M.-K., Harris, W.H., 1996. Monitoring the integrity of the cement—metal interface of total joint components in vitro using acoustic emission and ultrasound. J. Arthroplast. 11, 594–601.

Denard, P.J., Raiss, P., Sowa, B., Walch, G., 2013. Mid- to long-term follow-up of total shoulder arthroplasty using a keeled glenoid in young adults with primary glenohumeral arthritis. J. Shoulder Elb. Surg. 22, 894–900.

Dunne, N., 2008. 11 - mechanical properties of bone cements. In: Deb, S. (Ed.), Orthopaedic Bone Cements. Woodhead Publishing, pp. 233–264. https://doi.org/10.1533/9781845695170.3.233.

Gauci, M.O., et al., 2018. Anatomical total shoulder arthroplasty in young patients with osteoarthritis: all-polyethylene versus metal-backed glenoid. Bone Jt. J. 100-B, 485–492.

Gebert de Uhlenbrock, A., Püschel, V., Püschel, K., Morlock, M.M., Bishop, N.E., 2012. Influence of time in-situ and implant type on fixation strength of cemented tibial trays — a post mortem retrieval analysis. Clin. Biomech. 27, 929–935.

Gioe, T.J., Killeen, K.K., Grimm, K., Mehle, S., Scheltema, K., 2004. Why are total knee replacements revised?: analysis of early revision in a community knee implant registry. Clin. Orthop. Relat. Res. 428, 100–106, 1976-2007.

Hannon, C.P., Salih, R., Barrack, R.L., Nunley, R.M., 2023. Cementless versus cemented total knee arthroplasty: concise midterm results of a prospective randomized controlled trial. JBJS 105, 1430.

Hazelwood, K.J., et al., 2015. Case series report: early cement-implant interface fixation failure in total knee replacement. Knee 22, 424–428.

Heimbrook, A., Kelly, C., Gall, K., 2022a. Effects of 3D printed surface topography and normal force on implant expulsion. J. Mech. Behav. Biomed. Mater. 130, 105208.

Heimbrook, A., Kelly, C., Gall, K., 2022b. Interface contact behavior of 3D printed porous surfaces. J. Mater. Res. Technol. 21, 4115–4126.

Jones, M.D., Buckle, C.L., 2020. How does aseptic loosening occur and how can we prevent it? Orthop. Traumatol. 34, 146–152.

Karageorgiou, V., Kaplan, D., 2005. Porosity of 3D biomaterial scaffolds and osteogenesis. Biomaterials 26, 5474–5491.

Kasten, P., et al., 2023. Impact of polyethylene glenoid cementation technique on cement mantle integrity and stability after cyclic loading: a computed tomography and biomechanical study. J. Shoulder Elb. Surg. 32, 383–391.

Kelly, C.N., et al., 2019a. The effect of surface topography and porosity on the tensile fatigue of 3D printed Ti-6Al-4V fabricated by selective laser melting. Mater. Sci. Eng., C 98, 726–736.

Kelly, C.N., et al., 2019b. Fatigue behavior of As-built selective laser melted titanium scaffolds with sheet-based gyroid microarchitecture for bone tissue engineering. Acta Biomater. 94, 610–626.

Kelly, C.N., et al., 2021a. High-strength, porous additively manufactured implants with optimized mechanical osseointegration. Biomaterials 279, 121206.

Kelly, C.N., et al., 2021b. Functional repair of critically sized femoral defects treated with bioinspired titanium gyroid-sheet scaffolds. J. Mech. Behav. Biomed. Mater. 116, 104380.

Kirillova, A., Kelly, C., von Windheim, N., Gall, K., 2018. Bioinspired mineral–organic bioresorbable bone adhesive. Adv. Healthcare Mater. 7, 1800467.

Kopinski, J.E., Aggarwal, A., Nunley, R.M., Barrack, R.L., Nam, D., 2016. Failure at the tibial cement–implant interface with the use of high-viscosity cement in total knee arthroplasty. J. Arthroplast. 31, 2579–2582.

Kutzner, I., et al., 2018. Early aseptic loosening of a mobile-bearing total knee replacement: a case-control study with retrieval analyses. Acta Orthop. 89, 77–83.

Li, Y., Xiao, Y., Liu, C., 2017. The horizon of materiobiology: a perspective on material-guided cell behaviors and tissue engineering. Chem. Rev. 117, 4376–4421.

Lionberger, D., Wattenbarger, L., Conlon, C., Walker, T.J., 2020. Factors affecting aseptic loosening in primary total knee replacements: an in vitro study. J. Exp. Orthop. 7, 41.

Liu, Y., Rath, B., Tingart, M., Eschweiler, J., 2020. Role of implants surface modification in osseointegration: a systematic review. J. Biomed. Mater. Res. A 108, 470–484.

Mahmoud, D., Elbestawi, M.A., 2019. Selective laser melting of porosity graded lattice structures for bone implants. Int. J. Adv. Manuf. Technol. 100, 2915–2927.

Martin, J.R., Otero, J.E., Mason, J.B., Fehring, T.K., 2021. Where is the "Weak Link" of fixation in contemporary cemented total knee replacements? J. Arthroplast. 36, 2497–2501.

Nam, D., et al., 2019. Cemented versus cementless total knee arthroplasty of the same modern design: a prospective, randomized trial. J. Bone Joint Surg. Am. 101, 1185–1192.

Oosterom, R., Ahmed, T.J., Poulis, J.A., Bersee, H.E.N., 2006. Adhesion performance of UHMWPE after different surface modification techniques. Med. Eng. Phys. 28, 323–330.

Piper, C., Neviaser, A., 2022. Survivorship of anatomic total shoulder arthroplasty. JAAOS J. Am. Acad. Orthop. Surg. 30, 457.

Pittman, G.T., Peters, C.L., Hines, J.L., Bachus, K.N., 2006. Mechanical bond strength of the cement-tibial component interface in total knee arthroplasty. J. Arthroplast. 21, 883–888.

Raiss, P., et al., 2012. Results of cemented total shoulder replacement with a minimum Follow-up of ten years. JBJS 94, e171.

Refsum, A.M., et al., 2019. Cementing technique for primary knee arthroplasty: a scoping review. Acta Orthop. 90, 582–589.

Saha, S., Pal, S., 1984. Mechanical properties of bone cement: a review. J. Biomed. Mater. Res. 18, 435–462.

Sarah, J., et al., 2010. Failure mechanism of the all-polyethylene glenoid implant. J. Biomech. 43, 714–719.

Satalich, J.R., Lombardo, D.J., Newman, S., Golladay, G.J., Patel, N.K., 2022. Cementation in total hip arthroplasty: history, principles, and technique. EFORT Open Rev. 7, 747–757.

Sharkey, P.F., Lichstein, P.M., Shen, C., Tokarski, A.T., Parvizi, J., 2014. Why are total knee arthroplasties failing today—has anything changed after 10 years? J. Arthroplast. 29, 1774–1778.

Singh, N., et al., 2020. Selective laser manufacturing of Ti-based alloys and composites: impact of process parameters, application trends, and future prospects. Mater. Today Adv. 8, 100097.

Tapscott, D.C., Wottowa, C., 2024. Orthopedic implant materials. In: StatPearls. StatPearls Publishing, Treasure Island (FL).

Vaishya, R., Chauhan, M., Vaish, A., 2013. Bone cement. J. Clin. Orthop. Trauma 4, 157–163.

van Tol, A.F., Tibballs, J.E., Roar Gjerdet, N., Ellison, P., 2013. Experimental investigation of the effect of surface roughness on bone-cement-implant shear bond strength. J. Mech. Behav. Biomed. Mater. 28, 254–262.

Van Otten, T.J.M., Van Loon, C.J.M., 2022. Early aseptic loosening of the tibial component at the cement-implant interface in total knee arthroplasty: a narrative overview of potentially associated factors. Acta Orthop. Belg. 88, 103–111.

Vijayavenkataraman, S., Zhang, L., Zhang, S., Hsi Fuh, J.Y., Lu, W.F., 2018. Triply periodic minimal surfaces sheet scaffolds for tissue engineering applications: an optimization approach toward biomimetic scaffold design. ACS Appl. Bio Mater. 1, 259–269.

Wallace, A.L., Phillips, R.L., Macdougal, G.A., Walsh, W.R., Sonnabend, D.H., 1999. Resurfacing of the glenoid in total shoulder arthroplasty. A comparison, at a mean of five years, of prostheses inserted with and without cement. J. Bone Jt. Surg. 81, 510–518.

Wang, T., Pelletier, M.H., Bertollo, N., Crosky, A., Walsh, W.R., 2013. Cement-implant interface contamination: possible reason of inferior clinical outcomes for rough surface cemented stems. Open Orthop. J. 7, 250–257.

Zelle, J., Janssen, D., Peeters, S., Brouwer, C., Verdonschot, N., 2011. Mixed-mode failure strength of implant-cement interface specimens with varying surface roughness. J. Biomech. 44, 780–783.

Zhang, H., Brown, L.T., Blunt, L.A., Barrans, S.M., 2008. Influence of femoral stem surface finish on the apparent static shear strength at the stem–cement interface. J. Mech. Behav. Biomed. Mater. 1, 96–104.

Zhang, H., Brown, L., Blunt, L., 2009. A Better Understanding of the Surface Topography at the Stem-Cement Interface. American Society of Mechanical Engineers Digital Collection, pp. 513–515. https://doi.org/10.1115/IJTC2007-44019.